Matrix Converter Based on Trapezoidal Current Injection

Jiaxing Lei, *Member IEEE*, Xinlin Huang, Patrick Wheeler, *Fellow IEEE*, Yihui Xia, Jianfeng Zhao, Wu Chen

***Abstract*- The Matrix Converter (MC) is a direct AC-AC power converter featuring high power density and high efficiency. However, the conventional MC (CMC) topologies require high control complexity and high transistor capacity, hindering the wide applications. An emerging MC topology (3CI-MC) based on the third-harmonic current injection (3CI) reduces the control complexity, but require more transistors and complex clamping circuit. This paper proposes the trapezoidal current injection (TCI) technique to form a novel MC topology (TCI-MC), which consists of a line-commutated converter (LCC), a TCI circuit and a voltage source converter (VSC). Compared with the 3CI-MC, the proposed TCI-MC not only maintains the advantages of simple modulation and independent voltage control, but also achieves lower current stress on the LCC part of the circuit. The total transistor capacity of the proposed TCI-MC is the lowest among all the considered MC topologies. The clamping circuit is also simplified and the bidirectional switches are eliminated, reducing the implementation cost. Simulation and experimental results have verified the validity of the proposed topology.**

I. Introduction

AC-AC converters are widely used in industry applications, such as adjustable speed drives and renewable energy integration [1]-[2]. The typical AC-AC converter topology with bidirectional power flow capability is the back-to-back (B2B) converter, as shown in Fig. 1(a), which is composed of two voltage source converters (VSCs). The B2B converter features a simple structure and control. The cost is also relatively low. Yet, it requires bulky filter inductors and large DC-link capacitors [3]. Besides, the switching losses are relatively high, since all the devices work in PWM mode [4].

The matrix converter (MC), which achieves direct power conversion without intermediate energy storage elements, is considered a promising alternative to the B2B converter [5]-[6]. The conventional MC (CMC) topologies include the direct (DMC) and indirect (IMC) type [3], as shown in Fig. 1(b) and Fig. 1(c) respectively. Each bidirectional switch required by CMCs is usually constructed with two transistors. It has been demonstrated that CMCs can achieve much higher power density and efficiency than B2B converters [7]-[9]. Therefore, CMCs have received extensive and continuous attention for decades [10]-[12]. Nevertheless, the input and output control of CMCs are tightly coupled in the modulation, resulting in the complex switching sequences for normal operation. This is the side-effect of eliminating intermediate energy storage elements [13]. Besides, CMCs require 18 transistors handling the full power, resulting in much higher transistor VA capacity than the B2B converter [3]. Consequently, CMCs are often criticized for the higher complexity and cost compared to the B2B converter. These drawbacks have hindered the wide applications of CMCs.

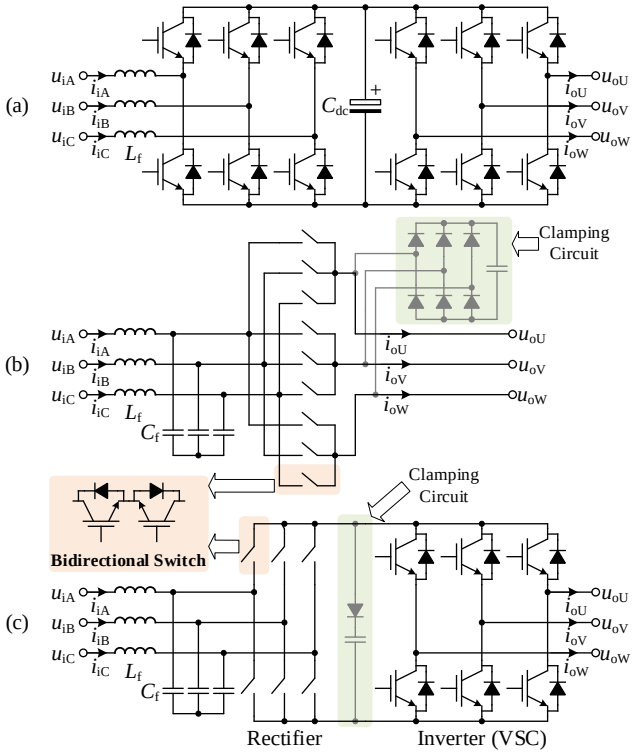

Fig. 1 (a) the typical back-to-back (B2B) converter; (b) the direct matrix converter (DMC); (c) the indirect matrix converter (IMC).

To improve the performance of CMCs, various advanced variants of MC topologies have been proposed in literature, mainly motivated by the physical two-stage feature of the IMC. In [14], the sparse MCs are proposed by modifying the rectifier stage of IMC, which reduces the transistor count but at the cost of higher conduction losses or losing bidirectional power flow capability. Incorporating the Z-source networks at the input or the DC-link of CMCs produces the topologies of Z-source MCs [15]-[16]. The Z-source MCs are able to boost the voltage utilization ratio [17], but the power density is reduced since some large passive components are used. Many other improved MC topologies can also be found in literature [18]-[21]. Though these topologies are advantageous in some specific applications, but the CMCs still dominate studies in the general cases.

In [22], a novel MC topology (3CI-MC) based on active third-harmonic current injection (3CI) is proposed, as shown in Fig. 2(a). The 3CI-MC can be derived by replacing the rectifier stage of IMC with a line-commutated converter (LCC) and a 3CI circuit in parallel. The LCC handles the main power flow while the 3CI compensates the harmonics generated by the LCC. The 3CI technique had been adopted in rectifier applications to promote the converter efficiency [23]. According to [22], the 3CI-MC not only maintains the major

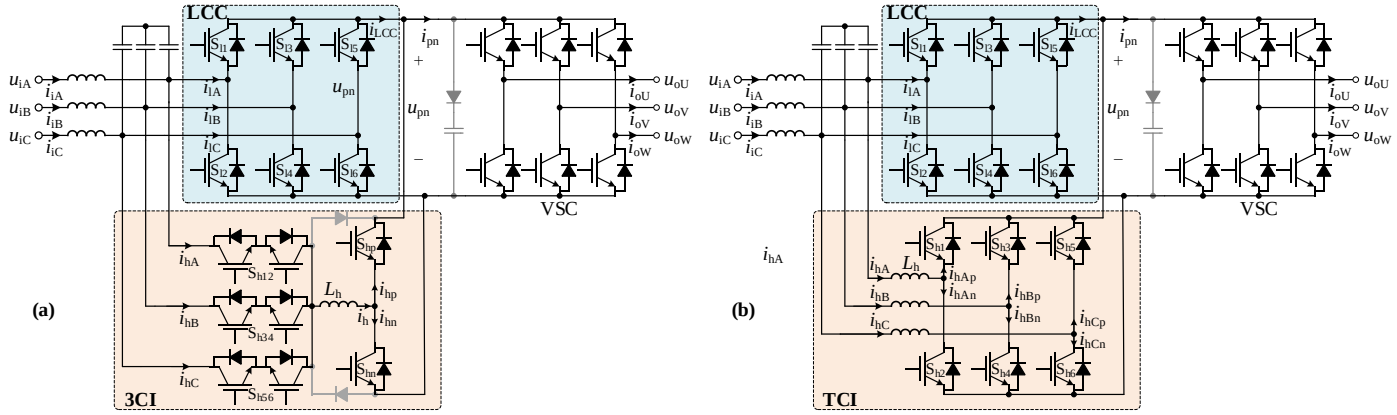

Fig. 2 Topologies of matrix converter based on (a) active third-harmonic current injection (3CI); (b) trapezoidal current injection (TCI).

features of CMCs, but also achieves much lower control complexity since the input and output control can be easily decoupled in the modulation. No complex switching sequence is required by 3CI-MC. Also, the current stress of the 3CI circuit is only half of the input current amplitude. In recent years, progress was made with the 3CI-MC, further improving its performance. In [24] and [25], the 3CI-MC with multiple output-stage VSCs and the three-level T-type 3CI-MC are proposed. In [26], the input current distortion at the sector boundary is suppressed by adding a LC filter in the DC-link. In [27] and [28], improved 3CI-MC topologies with auxiliary switches are proposed to extend the control range of input reactive power.

The advantages of 3CI-MC prove that it is a promising MC topology. Motivated by the concept of 3CI technique, this paper proposes a trapezoidal current injection (TCI) technique and applies it to replace the 3CI technique, forming a novel MC topology (TCI-MC), as shown in Fig. 2(b). Compared with the emerging 3CI-MC, the proposed TCI-MC not only maintains its superior control performance, but also offers more advantages:

- Transistor count is reduced from 20 to 18.
- Clamping circuit is simplified with two fewer diodes.
- The LCC part has lower current stress.
- The total transistor capacity is reduced.
- Bidirectional switches are eliminated.

The rest of this paper is organized as follows: Section II introduces the operation and control of the proposed TCI-MC; Section III presents power loss analysis; Section IV shows the comparison with other AC-AC topologies; Section V provides the simulation and experimental results. Section VI draws the conclusion.

II. Operation and Control of TCI−MC

A. Topology Description

As shown in Fig. 2(b), the proposed topology is composed of three three-phase bridges which act as the LCC, TCI, and VSC. These three parts share the common DC-link without energy storage elements. An LC filter is placed at the input side of LCC, and hence the input of LCC should be considered as a three-phase voltage source imposed by the filter capacitors. Together with the three-phase input filter inductors L_h, the TCI is placed in parallel with the LCC. It should be noted that although the LCC and TCI have the same transistor configuration as the VSC, both of them are not fully controllable VSCs, because the electrical characteristics of the input and the DC-link of them are quite different to the typical VSC. If bidirectional power flow capability is not required, the LCC could be replaced with a simple three-phase diode rectifier to reduce cost. The detailed operation principle of the topology will be presented in this section.

By comparing Fig. 2(a) and (b), it is clear that the TCI-MC and 3CI-MC have the same LCC and VSC parts, and the difference lies in the additional current injection circuit. The TCI-MC only requires 18 transistors, the same with CMCs but two less than the 3CI-MC. Besides, since the bridges always provide a path for the inductor current, the clamping circuit of the TCI-MC consists of only a diode and a capacitor, two diodes less than the 3CI-MC. The advantage of the proposed TCI-MC is the lower current stress in the LCC circuit. Together with the low current stress on the TCI circuit, the proposed topology requires the lowest transistor capacity among all the considered MC topologies.

B. Operation Principle of 3CI-MC

To better show how the proposed TCI-MC obtains sinusoidal input and output currents, the operation principle of 3CI-MC is firstly presented, its key waveforms are shown in Fig. 3. A comprehensive study of the 3CI technique can be refereed to [22] and [23].

Table I. Switching States of LCC and 3CI in the 3CI-MC

Sector	S_{l1}	S_{l2}	S_{l3}	S_{l4}	S_{l5}	S_{l6}	S_{h12}	S_{h34}	S_{h56}	S_{hp}	S_{hn}
I	1	0	0	0	0	1	0	1	0	**PWM**	
II	0	0	1	0	0	1	1	0	0	**PWM**	
III	0	1	1	0	0	0	0	0	1	**PWM**	
IV	0	1	0	0	1	0	0	1	0	**PWM**	
V	0	0	0	1	1	0	1	0	0	**PWM**	
VI	1	0	0	1	0	0	0	0	1	**PWM**	

Since the input of the LCC is a three-phase voltage source, the LCC cannot work in PWM mode. Switching states of the LCC in 3CI-MC are listed in Table I. In each input voltage sector, only the transistor in the upper arm corresponding to the maximum input voltage and the transistor in the lower arm corresponding to the minimum input voltage are turned on, while the rest transistors in the LCC maintain off. Therefore,

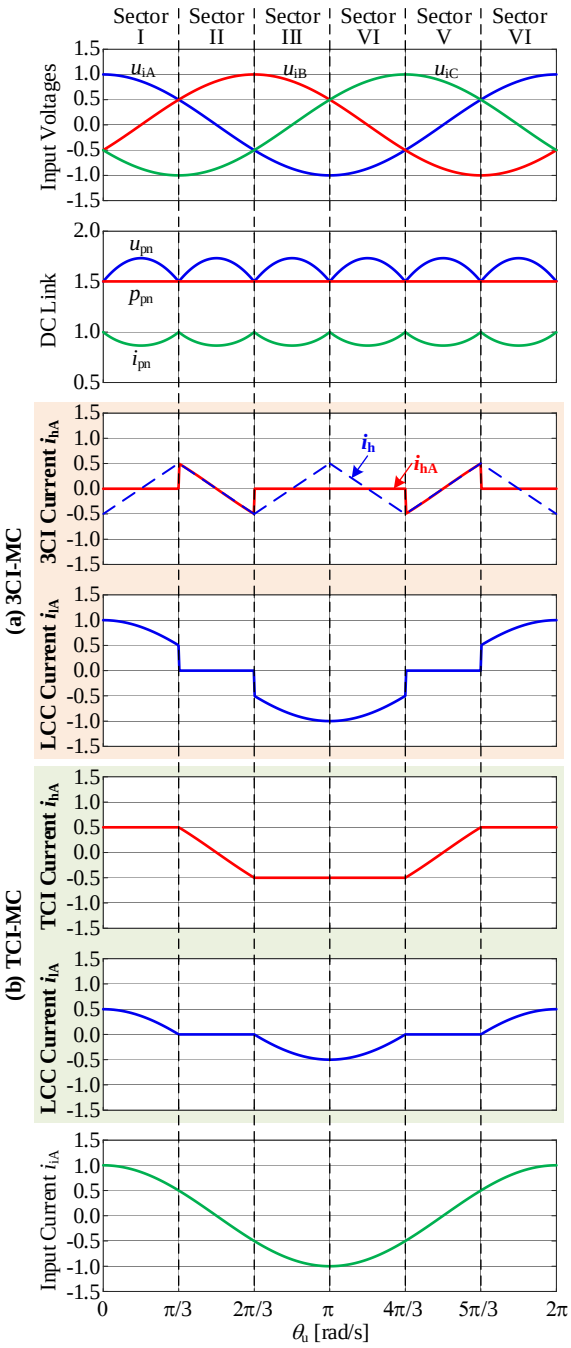

Fig. 3 Key waveforms (in p.u.) of the 3CI-MC and TCI-MC. All the terms represent only the low-frequency components. The input voltages, input currents, the DC-link voltage and current are the same for both converters.

the maximum input line-to-line voltage is always imposed on the DC-link of 3CI-MC. With the feedforward compensation of DC-link voltage fluctuation, the VSC part can generate balanced and sinusoidal output currents. In turn, the transferred active power p_{pn} on the DC-link is constant, the DC-link current i_{pn} fluctuates accordingly.

It is known that the LCC functions like a bidirectional diode rectifier. As a result, the LCC generates rich low-frequency harmonics in input currents if the 3CI circuit is disabled. Therefore, the objective of 3CI is to compensate for these low-frequency harmonics. According to [22]-[23], the reference current i_h^* of 3CI is always equal to the reference input phase current corresponding to the middle input voltage.

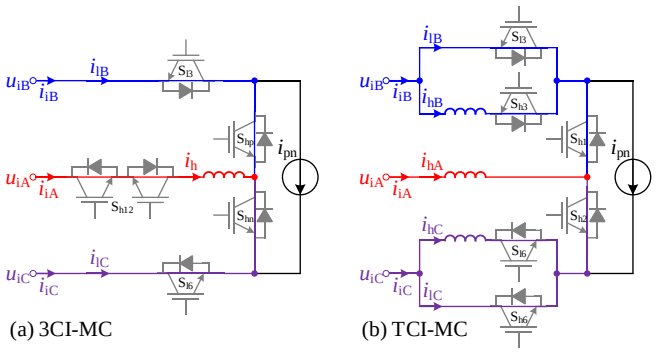

Fig. 4 Current flow paths of 3CI-MC and TCI-MC in sector II.

$$i_h^* = \begin{cases} i_{iA}^*, |u_{iB}| \geq |u_{iA}| \geq |u_{iC}| \text{ or } |u_{iC}| \geq |u_{iA}| \geq |u_{iB}| \\ i_{iB}^*, |u_{iA}| \geq |u_{iB}| \geq |u_{iC}| \text{ or } |u_{iC}| \geq |u_{iB}| \geq |u_{iA}| \\ i_{iC}^*, |u_{iA}| \geq |u_{iC}| \geq |u_{iB}| \text{ or } |u_{iB}| \geq |u_{iC}| \geq |u_{iA}| \end{cases}. \quad (1)$$

The half bridge is composed of S_{hp} and S_{hn}, which are fully controllable and work in a PWM mode. With closed-loop control, the actual i_h of 3CI tracks i_h^*.

It can be inferred from (1) that, when the three-phase reference input currents are sinusoidal, the waveform of i_h is close to a triangular wave, as shown in Fig. 3 (a). Each of the three bidirectional switches (i.e. S_{h12}, S_{h34}, and S_{h56}) in the 3CI circuit is switched on when the corresponding input voltage is the middle, as listed in Table I. Therefore, each phase current (e.g. i_{hA} in sector II) of 3CI only takes a part of i_h. The injected harmonic current i_h affects the LCC currents in a manner such that all the three-phase input currents i_{iA}, i_{iB}, i_{iC} realize sinusoidal [22]-[23].

C. Operation Principle of TCI-MC

In the proposed TCI-MC, the TCI circuit is composed of a three-phase bridge with a filter inductor for each input phase, which is similar to a VSC. However, each bridge in the TCI circuit is not always fully controllable, because the DC-link voltage of TCI-MC is not high enough. Each bridge therefore works in PWM mode only when the corresponding input voltage allows, while the switching state is fixed in the rest of the sectors. Switching states of LCC and TCI in TCI-MC are listed in Table II. The LCCs in TCI-MC and 3CI-MC have the same switching states.

Table II. Switching States of LCC and TCI in the TCI-MC

Sector	S_{l1}	S_{l2}	S_{l3}	S_{l4}	S_{l5}	S_{l6}	S_{h1}	S_{h2}	S_{h3}	S_{h4}	S_{h5}	S_{h6}
I	1	0	0	0	0	1	**1**	**0**	**PWM**		**0**	**1**
II	0	0	1	0	0	1	**PWM**		**1**	**0**	**0**	**1**
III	0	1	1	0	0	0	**0**	**1**	**1**	**0**	**PWM**	
IV	0	1	0	0	1	0	**0**	**1**	**PWM**		**1**	**0**
V	0	0	0	1	1	0	**PWM**		**0**	**1**	**1**	**0**
VI	1	0	0	1	0	0	**1**	**0**	**0**	**1**	**PWM**	

Taking sector II as an example to illustrate the operation principle of TCI-MC. In this sector, input voltages satisfy $u_{iB} \geq u_{iA} \geq u_{iC}$. Therefore, in the TCI circuit, transistors S_{h3} and S_{h6} are in the on-state while S_{h4} and S_{h5} are in the off-state

throughout sector II. The phase A bridge of the TCI is fully controllable, and thus S_{h1} and S_{h2} work in PWM mode. The current flow paths of 3CI-MC and TCI-MC in sector II are shown in Fig. 4.

The VSC part can be modelled as a current source i_{pn} at the DC-link. It is clear that, for input phase A, the current flow paths of 3CI-MC and TCI-MC are exactly the same if the voltage drops across the transistors are ignorable. Therefore, if PWM signals of S_{hp} and S_{hn} in the 3CI are applied to S_{h1} and S_{h2} in the TCI, the TCI-MC can obtain i_{iA} in the same way as 3CI-MC. Similarly, i_{iB} and i_{iC} in the TCI-MC are also the same as those in the 3CI-MC. Therefore, the proposed TCI-MC is able to achieve sinusoidal input currents, in the same manner as the 3CI-MC.

The key difference between the 3CI-MC and the TCI-MC is the input current distribution. When input voltages enter sector III from sector II, i_{hA} generated by the 3CI circuit drops to zero immediately since the bidirectional switch S_{h12} in 3CI-MC is turned off. However, for the TCI-MC, i_{hA} maintains constant in sector III, which can be inferred from the values of i_{hB} and i_{hC} in sector II. As shown in Fig. 4(b), voltage drops across the filter inductors of phase B and C are zero, assuming voltage drops across the transistors are negligible. As a result, i_{hB} and i_{hC} remain at their last values when the corresponding bridge works in PWM mode. Similarly, i_{hA} in sector III remains its last value in sector II. Therefore, i_{hA} presents the trapezoidal waveform throughout the six sectors, as shown in Fig. 3(b), which is the basis of the proposed technique.

From the above analysis it can be seen that i_{iA} is sinusoidal through the control of the TCI and i_{hA} is actively determined by the switching states of the TCI. Consequently, i_{lA} is passively determined by i_{iA} and i_{hA}, namely

$$i_{lA} = i_{iA} - i_{hA}, \tag{2}$$

where the capacitor current is ignored. As it can be seen from Fig. 3(b) and Fig. 4(b), the LCC and TCI in the TCI-MC share the input current stress. Therefore, compared with the 3CI-MC, the TCI-MC has more balanced current stress between LCC and TCI. This helps to improve the transistor utilization and reduce the total transistor capacity. The current stress will be further discussed in the Section IV.

D. Modulation and Control Strategy

The modulation algorithm and control strategy for the proposed TCI-MC can be translated from the 3CI-MC with minor modifications, as shown in Fig. 5. The switching states of the LCC and TCI (except the bridge working in PWM mode) can be directly determined based on Table II. Since the DC-link voltage of TCI-MC is not constant, feedforward compensation is used in the modulation of the VSC part. Namely, the instantaneous DC-link voltage u_{pn} is calculated based on the measured input voltages and then used for normalizing the modulation signals of VSC. The space vector pulse width modulation (SVPWM) is adopted for generating the gate signals of the VSC. Closed-loop control can be applied to the output currents if necessary.

Because only one bridge of the TCI works in PWM mode in each sector, the three-phase TCI currents can share one

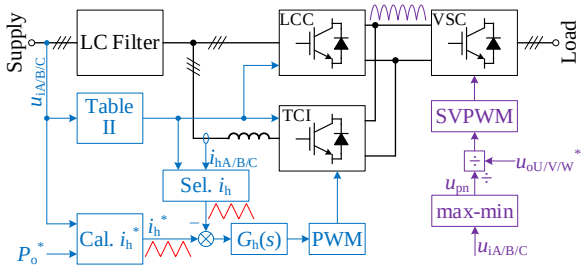

Fig. 5 Control strategy of the proposed TCI-MC

controller $G_h(s)$. The reference current i_h^* is calculated from the supply voltages and reference output active power P_o^*, which is exactly the same with that in the 3CI-MC [22]. The feedback signal i_h is selected from the three-phase TCI currents, depending on which phase bridge in the TCI works in PWM mode:

$$i_h = \begin{cases} i_{hA}, |u_{iB}| \ge |u_{iA}| \ge |u_{iC}| \ or \ |u_{iC}| \ge |u_{iA}| \ge |u_{iB}| \\ i_{hB}, |u_{iA}| \ge |u_{iB}| \ge |u_{iC}| \ or \ |u_{iC}| \ge |u_{iB}| \ge |u_{iA}| \\ i_{hC}, |u_{iA}| \ge |u_{iC}| \ge |u_{iB}| \ or \ |u_{iB}| \ge |u_{iC}| \ge |u_{iA}| \end{cases}. \tag{3}$$

As presented above, both i_h^* and i_h are triangular waves, which is the same as that in the 3CI-MC. The frequency of i_h^* is $3\omega_i$, and the main component of i_h^* is the 3th harmonic, where ω_i is the input angular frequency. Resonant controller is then adopted. Namely, the controller $G_h(s)$ is expressed as

$$G_h(s) = \frac{(k_{r1}s + k_{r2})(L_h s + R_h)}{s^2 + (3\omega_i)^2}, \tag{4}$$

where L_h and R_h are the inductance and parasitic resistance of the filter inductor for the TCI circuit; k_{r1} and k_{r2} are two parameters for adjusting the bandwidth.

III. Power Loss Analysis

This section presents the power loss analysis for both the 3CI-MC and TCI-MC. For simplicity, only the typical mode with forward power flow is considered, while the reverse power flow can be analyzed similarly. IGBTs are used for analysis. The MOSFETs may generate different results but the analysis method can be easily transplanted.

A. Semiconductor Losses

The average and RMS values of currents flowing through the semiconductor devices in the two converters are comparatively listed in Table III, where the current values of the 3CI-MC are provided by [22]. As for the TCI-MC, the current values of VSC are the same as those of the 3CI-MC. The difference lies in the current values of LCC and TCI, which can be calculated based on the waveforms shown in Fig. 3, where I_{DLCC} and I_{DTCI} represent the current flowing through the diodes in the LCC and TCI respectively; I_{STCI} represents the current flowing through the transistors in the TCI.

The conduction and switching loss of the semiconductor devices can be estimated by the current values and other parameters [22]:

$$P_{C,S} = I_{S,AVG} U_{CE0} + I_{S,RMS}^2 R_s, \tag{5}$$

Table III. Average and RMS values of the currents flowing through devices in the 3CI-MC and TCI-MC

Semiconductor devices		I_{AVG} (A)	I_{RMS} (A)
LCC of 3CI-MC	S_{li} (i=1~6)	0	0
	D_{li} (i=1~6)	$\frac{\sqrt{3}I_{im}}{2\pi}$	$I_{im}\sqrt{\frac{1}{6}+\frac{\sqrt{3}}{8\pi}}$
3CI	S_{h12}, S_{h34}, S_{h56}	$\frac{I_{im}\left(2-\sqrt{3}\right)}{2\pi}$	$I_{im}\sqrt{\frac{1}{12}-\frac{\sqrt{3}}{8\pi}}$
	S_{hp}, S_{hn}	$\frac{3I_{im}}{4\pi}\left(2-\sqrt{3}\ln 3\right)$	$I_{im}\sqrt{\frac{1}{8}+\frac{3\sqrt{3}}{4\pi}\ln\left(\frac{3}{4}\right)}$
	D_{hp}, D_{hn}	$\frac{3I_{im}}{4\pi}\left(2-2\sqrt{3}+\sqrt{3}\ln 3\right)$	$I_{im}\sqrt{\frac{1}{8}+\frac{3\sqrt{3}}{4\pi}\left(\ln\left(\frac{4}{3}\right)-\frac{1}{2}\right)}$
LCC of TCI-MC	S_{li} (i=1~6)	0	0
	D_{li} (i=1~6)	$\left(\frac{\sqrt{3}}{2\pi}-\frac{1}{6}\right)I_{im}$	$I_{im}\sqrt{\frac{1}{4}-\frac{3\sqrt{3}}{8\pi}}$
TCI	S_{hi} (i=1~6)	$\frac{I_{im}}{2\pi}\left(1-\frac{\sqrt{3}\ln 3}{2}\right)$	$I_{im}\sqrt{\frac{1}{24}+\frac{\sqrt{3}}{4\pi}\ln\left(\frac{3}{4}\right)}$
	D_{hi} (i=1~6)	$\frac{I_{im}}{2\pi}\left(\frac{\pi}{3}+1-\sqrt{3}+\frac{\sqrt{3}\ln 3}{2}\right)$	$I_{im}\sqrt{\frac{1}{8}+\frac{\sqrt{3}}{4\pi}\left(\ln\left(\frac{4}{3}\right)-\frac{1}{2}\right)}$
VSC of 3CI-MC and TCI-MC	S_{ip}, S_{in} (i=u, v, w)	$\frac{I_{om}}{2\pi}\left(1+\frac{\sqrt{3}q\cos\varphi_o}{2}\ln\left(2+\sqrt{3}\right)\right)$	$I_{om}\sqrt{\frac{1}{8}-\frac{q\cos\varphi_o}{8\pi}\left(\frac{9}{8}\ln 2-\frac{27}{16}\ln 3-\frac{5\sqrt{3}\pi}{16}\right)}$
	D_{ip}, D_{in} (i=u, v, w)	$\frac{I_{om}}{2\pi}\left(1-\frac{\sqrt{3}q\cos\varphi_o}{2}\ln\left(2+\sqrt{3}\right)\right)$	$I_{om}\sqrt{\frac{1}{8}+\frac{q\cos\varphi_o}{8\pi}\left(\frac{9}{8}\ln 2-\frac{27}{16}\ln 3-\frac{5\sqrt{3}\pi}{16}\right)}$

Note: I_{om} is the amplitude of output current; q is the voltage transfer radio; φ_o is the load power factor angle.

$$P_{S,S}=k_s U_{S,max} I_{S,AVG} f_s, \tag{6}$$

$$P_{C,D}=I_{D,AVG}U_{D0}+I_{D,RMS}^2 R_D, \tag{7}$$

where $P_{C,S}$, $P_{S,S}$ and $P_{C,D}$ are the conduction loss of IGBTs, the switching loss of IGBTs and the loss of diodes, respectively; U_{CE0} and U_{D0} are the forward voltage of IGBTs and diodes at zero current; R_s and R_D are the dynamic on-resistance of IGBTs and diodes; $I_{S,AVG}$, $I_{S,RMS}$, $I_{D,AVG}$ and $I_{D,RMS}$ are the average and RMS currents of IGBTs and diodes; $U_{S,max}$ is the voltage stress of IGBTs; k_s is the switching loss coefficient; f_s is the switching frequency. These parameters can be obtained from datasheets of the selected IGBT (Part No. IKY40N120CS6).

B. Inductor Losses

The inductor loss consists of two parts: the core loss and the parasitic resistor loss. With properly selected magnetic core, the core loss is neglected and only parasitic resistor loss is considered.

1) Loss of L_f: The current of L_f is the input current, so the parasitic resistor loss of L_f can be calculated as

$$P_{Lf}=\left(\frac{I_{im}}{\sqrt{2}}\right)^2 R_f=\frac{1}{2}I_{im}^2 R_f. \tag{8}$$

Eq. (8) is suitable for both 3CI-MC and TCI-MC.

2) Loss of L_h: The RMS value of i_h in 3CI-MC can be expressed as

$$I_{h\_RMS}=\sqrt{\frac{3}{\pi}\left(\int_{\frac{\pi}{3}}^{\frac{\pi}{2}} I_{im}^2\cos^2\theta d\theta\right)}=I_{im}\sqrt{\frac{1}{4}-\frac{3\sqrt{3}}{8\pi}} \tag{9}$$

Ignoring the inductor current change in the freewheeling mode, the RMS value of i_{hA} can be calculated as

$$\begin{aligned} I_{hA\_RMS}&=\sqrt{\frac{1}{\pi}\left[2\int_0^{\frac{\pi}{3}}\left(\frac{I_{im}}{2}\right)^2 d\theta+\int_{\frac{\pi}{3}}^{\frac{\pi}{2}} I_{im}^2\cos^2\theta d\theta\right]}\\ &=I_{im}\sqrt{\frac{1}{4}-\frac{\sqrt{3}}{8\pi}} \end{aligned} \tag{10}$$

The parasitic resistor losses in 3CI-MC and TCI-MC are obtained as

$$P_{Lh\_3CI\text{-}MC}=I_{h\_RMS}^2 R_h \approx 0.04 I_{im}^2 R_h \tag{11}$$

$$P_{Lh\_TCI\text{-}MC}=I_{hA\_RMS}^2 R_h \approx 0.18 I_{im}^2 R_h \tag{12}$$

C. *Quantitative Results*

Considering the same working conditions, the power losses of 3CI-MC and TCI-MC are listed in Table IV. The parameters used in analysis are the same with those provided in experiments.

It can be seen from Table IV that the proposed TCI-MC can achieve slightly lower power loss than 3CI-MC. This is mainly because the current stress on the LCC part is smaller. However, it should be noted that the quantitative results listed in Table IV are not of high precision. This is because the parameters for loss analysis are obtained from the figures of the device datasheet, which is not accurate enough. Besides, at

Table V Comparison between the proposed TCI-MC and other AC-AC converters

	TCI-MC	**3CI-MC**	**DMC**	**IMC**	**B2B**
Transistor Count	18	20	18	18	12
Bidirectional Switch Count	0	3	9	6	0
Transistor Voltage Stress	18: U_{ilm}	20: U_{ilm}	18: U_{ilm}	18: U_{ilm}	12: U_{pn}
Transistor Current Stress	12: I_{om}; 6: $0.5I_{im}$	6: I_{om}; 6: $I_{om}+0.5I_{im}$; 8: $0.5I_{im}$	18: I_{om}	18: I_{om}	6: I_{om}, 6: I_{im}
Total Transistor Capacity	$12U_{ilm}I_{om}+3U_{ilm}I_{im}$	$12U_{ilm}I_{om}+6U_{ilm}I_{im}$	$18U_{ilm}I_{om}$	$18U_{ilm}I_{om}$	$6U_{pn}I_{om}+6U_{pn}I_{im}$
Conduction Losses	Low	Low	Low	High	Low
Switching Losses	Low	Low	Low	Low	Very High
Additional Clamping Circuit	1 Diode 1 Capacitor	3 Diodes 1 Capacitor	6 Diodes 1 Capacitor	1 Diode 1 Capacitor	/
Modulation Complexity	Low	Low	High	Medium	Low
Max. Voltage Transfer Ratio	$\sqrt{3}/2$	$\sqrt{3}/2$	$\sqrt{3}\cos\varphi_i/2$	$\sqrt{3}\cos\varphi_i/2$	$\geqslant 1$
DC-link Capacitors	No	No	No	No	Large
Input Filter Components	$3L_f+3C_f+3L_h$	$3L_f+3C_f+1L_h$	$3L_f+3C_f$	$3L_f+3C_f$	$3L_f$

Note: Comparison among DMC, IMC and B2B can be referred to [7]. The comparison in this table is made incrementally. φ_i is the input power factor angle.

every point of the MC systems, the voltage or current is not constant DC-signal. This means the power loss is always time-variable. Moreover, the power loss of a practical converter depends on many other factors, such as temperature, PCB wiring, gate drivers, parameter mismatch, and etc. To the best knowledge of authors, the mismatch between theoretical loss analysis and experiments is very common in publications of MCs. Yet, the presented analysis process still has reference value to show the differences between 3CI-MC and TCI-MC, if more accurate parameters of the semiconductor devices are available.

Table IV. Power Losses of the 3CI-MC and TCI-MC

			3CI-MC	**TCI-MC**
Semiconductor losses	LCC	$P_{C,S}$	0 W	0 W
		$P_{S,S}$	0 W	0 W
		$P_{C,D}$	24.47 W	8.64 W
		Total	24.47 W	8.64 W
	3CI or TCI	$P_{C,S}$	16.66 W	8.52 W
		$P_{S,S}$	12.43 W	12.68 W
		$P_{C,D}$	10.85 W	26.91 W
		Total	39.94 W	48.11 W
	VSC	$P_{C,S}$	8.92 W	8.92 W
		$P_{S,S}$	65.14 W	65.14 W
		$P_{C,D}$	3.77 W	3.77 W
		Total	77.83 W	77.83 W
	Total		142.24 W	134.58 W
Inductor Losses			9.65 W	12.76 W
Total Losses			151.89 W	147.34 W
Rated power			5.76 kW	5.76 kW
Calculated Efficiency			97.36%	97.44%

IV. Comparison with Other AC-AC Converters

To highlight the advantages and disadvantages, this section further makes the comparison between the proposed TCI-MC with other AC-AC converters. The selected MC include the 3CI-MC, DMC and IMC as they have similar features with the proposed TCI-MC. The closest rival is the 3CI-MC. The comparison is considered for general applications. Other MC topologies which have different features are not considered. In addition, the widely used B2B converter is included in the comparison. Since the comprehensive comparison between DMC, IMC and B2B has been made in [7], the comparison in this section is made incrementally. The results are listed in Table V. The next sections will show the detailed comparison for some key aspects.

A. Transistor Count

It can be seen from Fig. 1 and Fig. 2(b) that the TCI-MC and CMCs require 18 transistors, the 3CI-MC requires 20 transistors, while the B2B requires only 12 transistors. Usually, a transistor should be used in the clamping circuit for discharging the clamping capacitors. However, it has small capacity and thus is omitted.

Note that the bidirectional switch is indispensable in CMCs and 3CI-MC. Theoretically, this is not an issue for the operating performance. Yet, the bidirectional switch module is far less common than the half-bridge module in commercial market. From this point of view, compared with other MC topologies, the proposed TCI-MC is able to reduce the implementation cost since it can be constructed with nine half-bridge modules.

B. Voltage Stress

Like CMCs, all the transistors in the TCI-MC need to withstand the maximum input line-to-line (L-L) voltage. Therefore, the voltage stresses of CMCs and TCI-MC are all U_{ilm} which denotes the amplitude of input L-L voltage.

For 3CI-MC, the LCC part, the VSC part and the half-bridge in the 3CI circuit also need to withstand the maximum input L-L voltage. With proper modulation, bidirectional switches in the 3CI circuit only need to withstand the minimum input (L-L) voltage. This means that the voltage stress on the 3CI circuit is only $0.866U_{ilm}$. Yet, selection of these transistors must consider the worst and unpredictable cases. As a result, it is reasonable to assume that the voltage stress of all the transistors in 3CI-MC is also U_{ilm}.

All the considered MC topologies have lower voltage stress than the B2B converter, since the latter has to withstand the maximum DC-link voltage U_{pn}. For linear modulation, the u_{pn}

of B2B should be higher than U_{ilm} in practice, e.g. U_{pn} = $1.1U_{ilm}$.

C. Current Stress

In this paper, the current stress on a transistor is defined as the maximum current flowing through it. For CMCs, the current stress is determined by the output current amplitude I_{om}. For the 3CI-MC and TCI-MC, the current stresses on the 3CI and TCI are the amplitude of the injected harmonic current, which is only $0.5I_{im}$ where I_{im} is the input current amplitude.

The difference between 3CI-MC and TCI-MC lies in the current stress on the LCC parts. As shown in Fig. 2, the output current i_{LCC} of LCC in 3CI-MC can be expressed as

$$i_{LCC} = i_{pn} - i_{hp}, \tag{13}$$

where i_{pn} is the DC-link current flowing into the VSC; i_{hp} is the current flowing though the transistor S_{hp}. Due to the lack of DC-link filter components, i_{pn} has the pulsed waveform of which the maximum is the output current amplitude I_{om} and the minimum is zero. Certainly, this is only true for the unity output power factor. Under a non-unity output power factor, the maximum and minimum of i_{pn} could be different, but the analysis can be handily extended. Like i_{pn}, i_{hp} is pulsed between i_h and 0. Since i_h is a triangular waveform with an amplitude of $0.5I_{im}$, the maximum of i_{hp} is $0.5I_{im}$ while the minimum is $-0.5I_{im}$. Therefore, the current stress on the LCC in the 3CI-MC can be obtained

$$I_{LCC,peak} = \max\left(i_{pn}\right) - \min\left(i_{hp}\right) = I_{om} + 0.5I_{im}. \tag{14}$$

As shown in Fig. 2(b), i_{LCC} in the TCI-MC is expressed as

$$i_{LCC} = i_{pn} - \left(i_{hAp} + i_{hBp} + i_{hCp}\right) = i_{pn} - i_{hTp}, \tag{15}$$

where i_{hAp}, i_{hBp} and i_{hCp} are currents flowing through S_{h1}, S_{h3} and S_{h5} respectively; i_{hTp} is the sum of i_{hAp}, i_{hBp} and i_{hCp}. According to the operation principle of TCI-MC, in each sector, there will be always one current of i_{hAp}, i_{hBp} and i_{hCp} that maintains $0.5I_{im}$, one current is the pulsed triangular waveform of which the amplitude is $0.5I_{im}$, and the rest one is zero. This means that the maximum of i_{hTp} is I_{im} and the minimum is zero. Therefore, the current stress on the LCC part of the TCI-MC can be obtained as

$$I_{LCC,peak} = \max\left(i_{pn}\right) - \min\left(i_{hTp}\right) = I_{om}. \tag{16}$$

(14) and (16) indicate that, compared with the 3CI-MC, the proposed TCI-MC has lower current stress on the LCC part, while the current stresses on the rest circuits are not changed.

Note that, the above analysis ignores the parasitic resistance of the filter inductors. In practice, the TCI current would drop slowly in the desired flat area, subject to the time constant of the filter inductor. This will influence the current distribution and the current stress. However, the total input currents (i_{iA}, i_{iB} and i_{iC}) are not influenced and can still achieve sinusoidal, since they are determined by the control of the TCI circuit. Besides, the proposed topology is still able to reduce the current stress on the LCC circuit, since the TCI always shares the current stress between the devices.

D. Total Transistor Capacity (TTC)

The total transistor capacity (TTC) of a converter is an important factor influencing the cost. The TTC is related with the transistor count N, the voltage rating and current rating. For simplicity, the TTC index is defined as

$$\mathrm{TTC} = \sum_{i=1}^{N} U_{\mathrm{R}i} I_{\mathrm{R}i}, \tag{17}$$

where U_{Ri} and I_{Ri} are the voltage rating and current rating of the ith transistor respectively.

Usually, U_{Ri} and I_{Ri} are proportional to the voltage stress and current stress respectively. The proportional gain reflects the capacity margin for safe operation. Herein, the gain is considered as unity for simplicity. The TTC can be then calculated for each converter according to the discussion presented in part B and part C of this section. The results are listed in the 6th row of Table V. Note that, for MCs, I_{im} should be less than $0.866I_{om}$ in the linear modulation region [7]. It is clear that the TTC of TCI-MC is the lowest among all the MC topologies, which is the benefit of the lower current stress on LCC. Besides, the TTC of TCI-MC approaches that of B2B, indicating that the proposed topology has narrowed the gap between MCs and B2B in terms of transistor cost.

E. Power Loss

The analysis in Section III shows that the TCI-MC generates slightly lower power loss than the 3CI-MC. This part will further compare them with the CMCs and B2B. Note that more rigorous analysis about CMCs and B2B has been provided in [7]. Due to the limited space, the quantitative analysis about CMCs and B2B are not presented in this paper. Yet, the qualitative discussion is sufficient to get the valuable conclusion.

1) Conduction loss: For a converter, the conduction loss is mainly determined by the count of transistors on the current flow path. Clearly, both the DMC and B2B have very low conduction losses, since only four transistors are located on the current flow path from input side to output side. The conduction loss of IMC is much higher because six transistors are on the path. For 3CI-MC, the 3CI and VSC handle the major power and four transistors are on the path. Though there are more transistors on the current low path of 3CI, the injected current is very small. From this point of view, the conduction loss of 3CI-MC is slightly higher than the DMC, but the difference is ignorable in the total power loss. For the proposed TCI-MC, fewer transistors are in the flow path of the injected harmonic current, as shown in Fig. 4(b). Therefore, the conduction loss of TCI-MC is lower than 3CI-MC. From the input to output, it can be approximately considered that only four transistors are located on the current flow path, despite that some currents have different low path. Therefore, the TCI-MC also has low conduction loss, just like the DMC and B2B.

2) Switching loss: According to the operation principle of 3CI-MC and TCI-MC, they have quite close switching loss which is mainly contributed by the VSC part. Note that, the VSC part is similar to the inverter stage of IMC. Therefore, it can be inferred that the switching loss of 3CI-MC and TCI-MC are slightly higher than IMC, as the input stage of IMC

can achieve zero-current switching [7]. Yet, the injected harmonic current is very small and thus the switching loss of 3CI and TCI circuits only account for a small portion in the total power loss. Therefore, the switching loss of 3CI-MC and TCI-MC is close to the CMCs. They can all achieve much higher efficiency than B2B as both stages of B2B work in hard-switching mode with high chopping current.

3) Inductor loss: Since the 3CI-MC and TCI-MC requires more filter inductors for the harmonic injection circuit, they generate more inductor losses than the CMCs. However, since the inductors in B2B are much larger than that required by MCs, the differences among 3CI-MC, TCI-MC and CMCs are ignorable.

Based on the above analysis, it can be known that the DMC is the most efficient topology. The 3CI-MC and TCI-MC are less efficient than DMC, but is more efficient than IMC. Yet, all the MC topologies can be considered high-efficiency AC-AC converters compared with the B2B, which is consistent with the study in [7].

F. Passive Components

It was shown in [7] that the passive components of CMCs could be significantly smaller than the B2B, contributing to the higher power density of CMCs. Compared with CMCs, a 3CI-MC requires one additional filter inductor while the TCI-MC requires three. The design of these inductors is presented in [22]. This is the major drawback of the proposed TCI-MC compared with CMCs and 3CI-MC. In practice, a small filter inductor L_h is used since the amplitude of the injected harmonic current is only half of the input current amplitude. Moreover, reducing L_h would not deteriorate the input power quality since the input LC filter is sufficient to attenuate the high-frequency harmonics. Therefore, considering the advantages of the TCI-MC, the cost of the small additional filter inductors is worthy.

G. Summary

From the analysis in section II and the comparison in this section, it can be seen that the proposed TCI-MC inherits the advantages of the 3CI-MC, including lower modulation complexity and independent output voltage control. Besides, it has reduced the current stress of the LCC part and further the total transistor capacity, simplified the clamping circuit and eliminated the bidirectional switches. Other merits of TCI-MC and 3CI-MC are similar to the CMCs. Therefore, it can be concluded that the proposed TCI-MC is a promising MC topology with superior comprehensive performance.

V. Simulation and Experimental Results

A. Simulation and Experimental Parameters

To verify the effectiveness of the proposed TCI technique, a TCI-MC prototype has been constructed, as shown in Fig. 6. Parameters of the prototype are provided in Table VI. For comparison, the 3CI-MC was constructed by replacing the TCI part with a 3CI circuit, the experimental parameters are the same with TCI-MC. The rated output current amplitude is 16 A, and the corresponding rated power is 5.76 kW. A PI-based closed-loop control is applied to the output currents in the synchronous reference frame. A Chroma 61845 programmable AC source acts as the power supply.

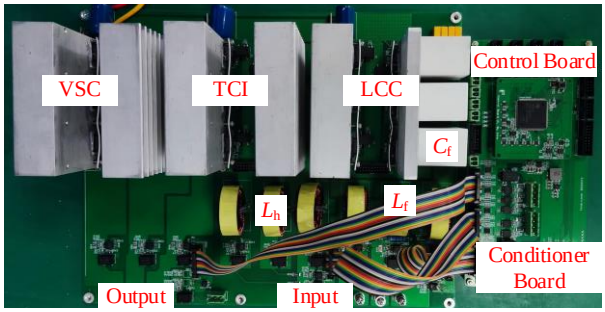

Fig. 6 Experimental prototype of TCI-MC.

Since the input currents of the LCC after the filter capacitors are unavailable in practice. Simulation verification is also implemented to show the current stress comparison. The simulation parameters are the same as the experimental parameters, except that ideal transistors and filter components were used in the simulation.

TABLE VI Experimental Parameters

Variables	Description	Values
U_s	Nominal Input Voltage (Phase RMS)	220 V
f_i	Nominal Input Frequency	50 Hz
I_{om}	Nominal Amplitude of Output Current	16 A
f_o	Nominal Output Frequency	50 Hz
L_f	Input Filter Inductor	1 mH
R_f	Resistance of L_f	0.04 Ω
C_f	Input Filter Capacitor	15 μF
R_d	Damping Resistor of the Input Filter	15 Ω
L_h	Filter Inductor for the Injection Circuit	1 mH
R_h	Resistance of L_h	0.04 Ω
L_o	Output Inductor	2 mH
R_o	Output Resistor	15 Ω
IGBT	Power Switches	IKY40N120CS6
DSP	Digital Signal Processor	TMS320F28379D
f_{sw}	Switching Frequency	16 kHz
f_{sa}	Sampling Frequency	32 kHz
K_{r1}	First parameter of $G_h(s)$	1.26×10^4
K_{r2}	Second parameter of $G_h(s)$	3.86×10^7

B. Simulation Results

The simulation results are shown in Fig. 7. It can be seen that, the TCI-MC obtains exactly the same input and output currents as the 3CI-MC. Both topologies achieve sinusoidal currents at the input and output sides. The key differences between the two topologies lie in the currents of the LCC and the harmonic current injection circuit. In the 3CI-MC, the 3CI current i_{hA} drops to zero immediately when the corresponding phase voltage u_{sA} becomes maximum or minimum. The amplitude of the LCC current i_{lA} after the filter capacitor is up to 22 A, which is consistent with the theoretical analysis presented in (14). The i_{lA} before the filter capacitor represents its low-frequency component plus the high-frequency component in i_{hA}. It can be shown that the amplitude of the low-frequency component of i_{lA} is about 12.5A, the same with the amplitude of the input current i_{iA}.

In the TCI-MC, the TCI current i_{hA} maintains its last value when the corresponding phase voltage u_{sA} becomes maximum

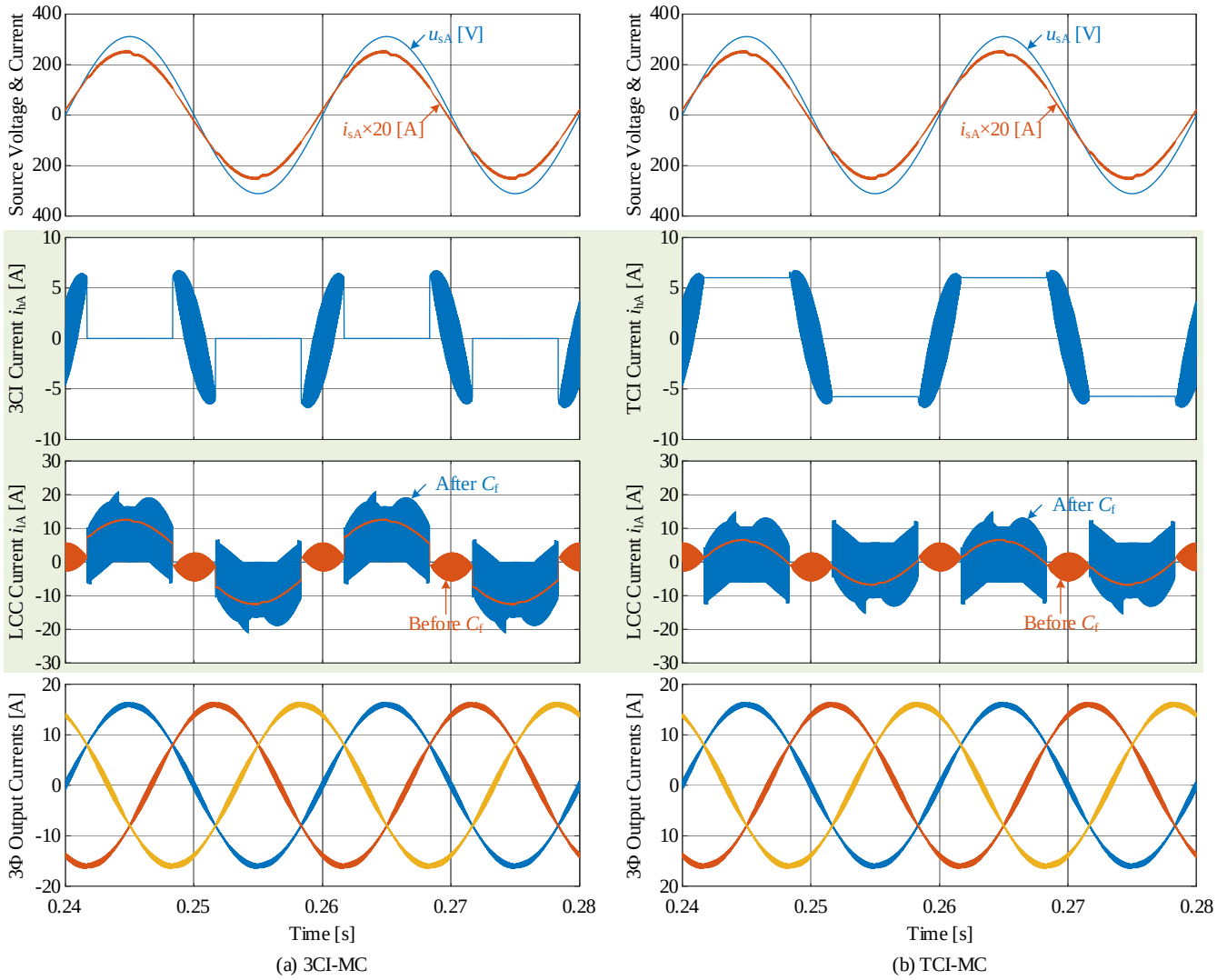

Fig. 7 Simulation results of (a) 3CI-MC and (b) TCI-MC. Ideal transistors and filter components are adopted in simulation.

or minimum. i_{hA} presents the trapezoidal waveform, except some high-frequency components are observed when the corresponding voltage is the middle. It can be seen that the amplitude of i_{lA} after the capacitor is 16A, the same as the output current amplitude. Besides, the amplitude of i_{lA} before the capacitor is only 6.25A, half of the amplitude of the input current i_{iA}.

The simulation results have verified that the proposed TCI-MC can achieve the same input and output control performance as the emerging 3CI-MC, but the current stress between the LCC and TCI is more balanced. The current stress on the LCC part is lower than that in the 3CI-MC.

C. *Experimental Results*

Experimental results of the 3CI-MC and TCI-MC are shown in Fig. 8 (a) and (b). The filter capacitors are placed as close as to the input of LCC, only the current i_{lA} before the filter capacitor C_f is presented. It can be seen that the input and output currents of both the 3CI-MC and TCI-MC are highly sinusoidal. For 3CI-MC, the THDs of i_{iA} and i_{oU} are 3.48% and 3.71% respectively. For TCI-MC, the THDs become 3.35% and 3.77%. Therefore, the two topologies can achieve commensurate steady-state control performance.

The key differences between the two topologies lie in the waveforms of i_{lA} and i_{hA}. For 3CI-MC, because i_{hA} drops to zero when u_{sA} is maximum or minimum among all the three-phase voltages, the amplitude of i_{lA} is the same with i_{iA}. On the contrary, the i_{hA} of the TCI-MC in this period is not zero, and thus i_{lA} is much lower than i_{iA}. This means the current stress on the LCC part stress is reduced. Note i_{hA} decreases gradually in this period, resulting from the non-zero resistance of the filter inductors. This will also affect the waveform of i_{lA}. Even so, the amplitude of i_{lA} in the TCI-MC is still much lower than for the 3CI-MC.

By changing the reference amplitude of output current, the efficiency curves of 3CI-MC and TCI-MC can be obtained as shown in Fig. 9. It can be seen that the efficiencies are quite close to each other. The efficiency under nominal load is 96.98% for 3CI-MC and 97.04% for TCI-MC. The measured efficiency is slightly lower than calculated. This is because the prototype efficiency is affected by many other factors, such as temperature, PCB wiring, gate drivers, parameter mismatch,

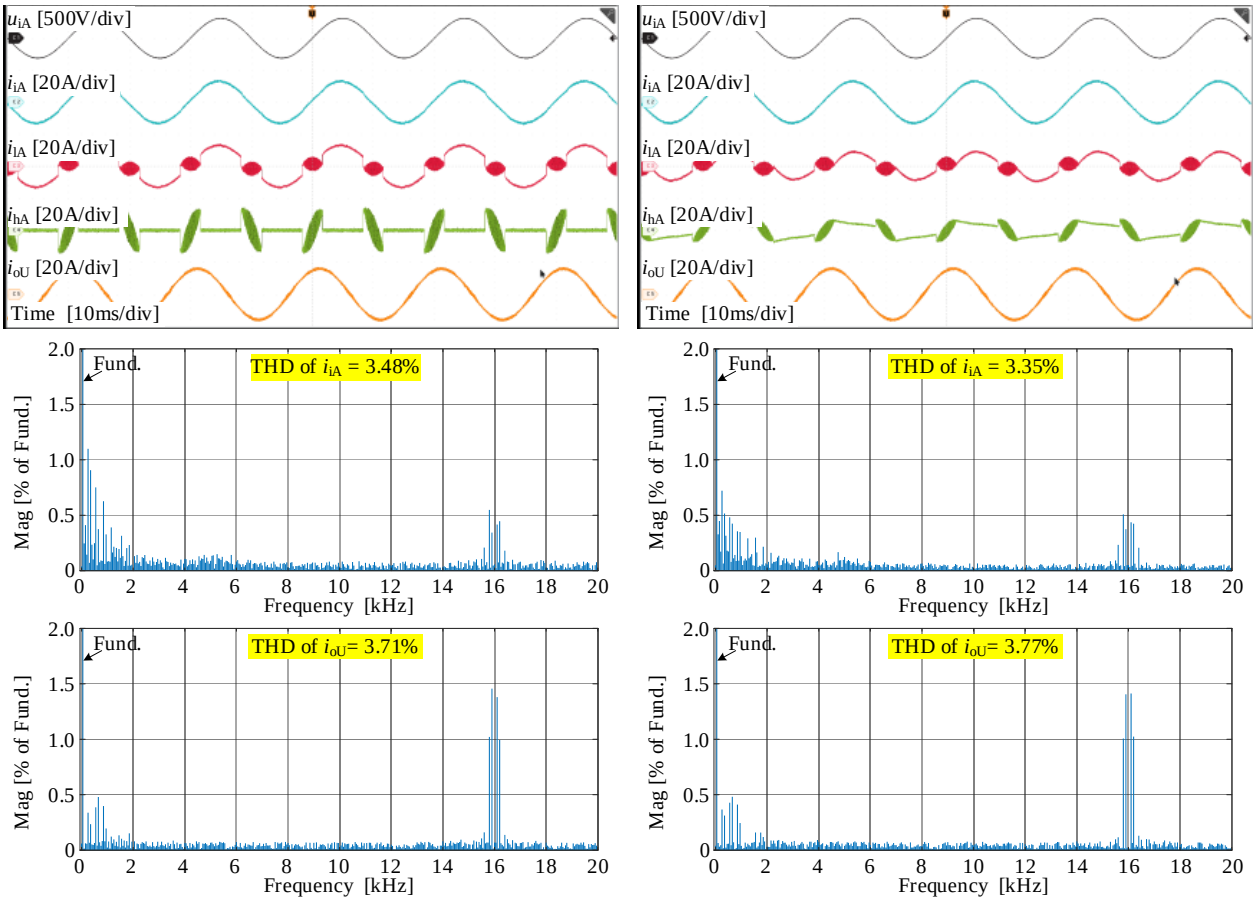

(a) 3CI-MC (b) TCI-MC

Fig. 8 Experimental results of (a) 3CI-MC and (b) TCI-MC at the steady-state.

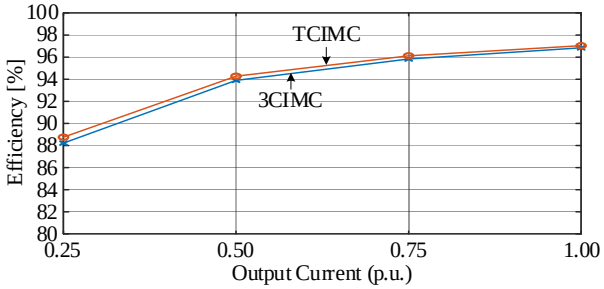

Fig. 9 Efficiency of 3CI-MC and TCI-MC under different output currents.

and etc. Considering the measurement error, such difference is ignorable. This is mainly because the conduction loss difference between the input stages of 3CI-MC and TCI-MC is limited and thus is concealed in the total converter loss. Anyhow, Fig. 9 proves that both TCI-MC and 3CI-MC can achieve relatively high efficiency.

Fig. 10 shows the experimental results when the input voltages are disturbed by 5% fundamental negative sequence component, 5% 5th harmonic and 5% 7th harmonic. The considered disturbances cover the most common disturbances in practice. It can be seen that, both the 3CI-MC and TCI-MC could achieve highly sinusoidal output currents even under the severe input disturbances, proving the performance of the two topologies with the associated control strategy. The input currents are distorted, resulting from the lack of energy storage elements. This is a common issue for the MC topologies. Anyhow, Fig. 10 has verified the effectiveness of the proposed topology under input voltage disturbances.

Experimental results when the output current amplitude steps from 8 A to 16 A are presented in Fig. 11. It can be seen that the two topologies have quite close dynamic control performance at both the input and output side. Therefore, the proposed topology will not affect the dynamic performance. Note the i_{hA} will drop to zero if the output current is small. This is because of the power dissipation caused by the parasitic resistance of the filter inductor. Yet, i_{hA} maintains large value when the output current is high. Therefore, the current stress on the LCC part is still reduced, despite of the degradation of i_{hA} in the desired flat area.

VI. Conclusions

With the proposed trapezoidal current injection technique, a novel TCI-MC topology is proposed. As demonstrated by simulation and experimental results, the proposed TCI-MC can reduce the transistor count, hardware complexity, current stress and the total transistor VA capacity. Therefore, it is a stronger competitor than the emerging 3CI-MC and the CMCs to the common B2B converter. For the proposed TCI-MC, optimizing the input filter parameters would be a meaningful work to decrease the adverse effect of the additional inductors.

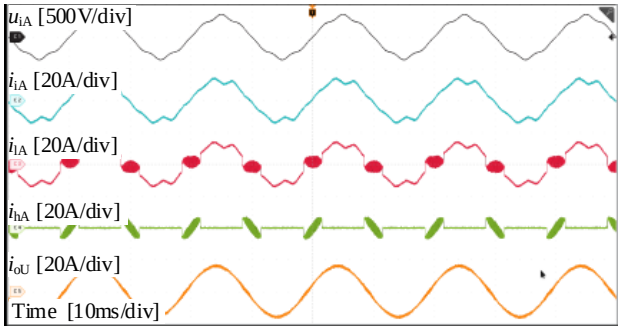

(a) 3CIMC

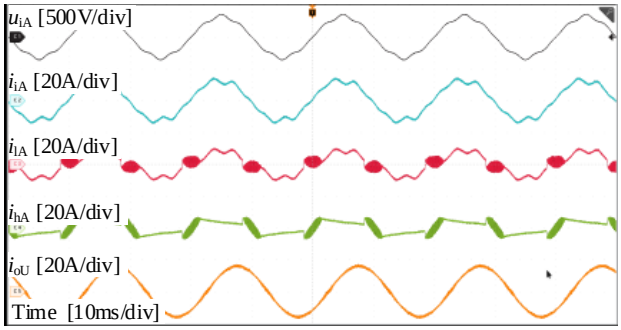

(b) TCIMC

Fig. 10 Experimental results of (a) 3CI-MC and (b) TCI-MC when the input voltages are disturbed by 5% fundamental negative sequence component, 5% 5th harmonic and 5% 7th harmonic

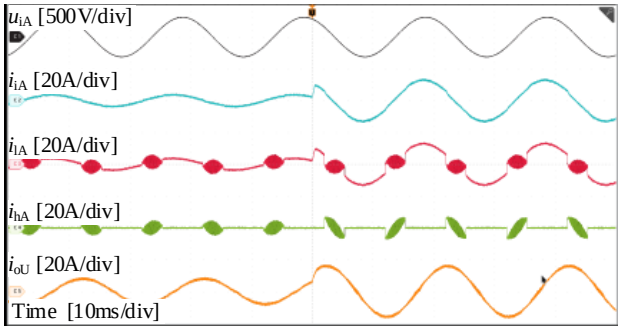

(a) 3CIMC

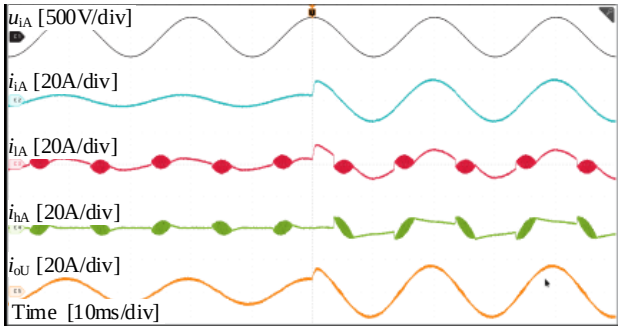

(b) TCIMC

Fig. 11 Experimental results of (a) 3CI-MC and (b) TCI-MC when the output current amplitude steps from 8 A to 16 A.

VI. Reference

[1] J. W. Kolar and J. Huber, "Next-Generation SiC/GaN Three-Phase Variable-Speed Drive Inverter Concepts," in *PCIM Europe digital days 2021; International Exhibition and Conference for Power Electronics, Intelligent Motion, Renewable Energy and Energy Management*, 2021, pp. 1-5.

[2] Z. Tang, Y. Yang and F. Blaabjerg, "Power electronics: The enabling technology for renewable energy integration," *CSEE Journal of Power and Energy Systems*, vol. 8, no. 1, pp. 39-52, Jan. 2022.

[3] J. W. Kolar, T. Friedli, J. Rodriguez and P. W. Wheeler, "Review of Three-Phase PWM AC–AC Converter Topologies," *IEEE Trans. Ind. Electron.*, vol. 58, no. 11, pp. 4988-5006, Nov. 2011.

[4] K. Shi, A. Zhao, J. Deng and D. Xu, "Zero-Voltage-Switching SiC-MOSFET Three-Phase Four-Wire Back-to-Back Converter," *IEEE J. Emerg. Sel. Topics Power Electron.*, vol. 7, no. 2, pp. 722-735, June. 2019.

[5] L. Empringham, J. W. Kolar, J. Rodriguez, P. W. Wheeler and J. C. Clare, "Technological Issues and Industrial Application of Matrix Converters: A Review," *IEEE Trans. Ind. Electron.*, vol. 60, no. 10, pp. 4260-4271, Oct. 2013.

[6] J. Zhang, L. Li and D. G. Dorrell, "Control and applications of direct matrix converters: A review," *Chinese Journal of Electrical Engineering*, vol. 4, no. 2, pp. 18-27, June. 2018.

[7] T. Friedli, J. W. Kolar, J. Rodriguez and P. W. Wheeler, "Comparative Evaluation of Three-Phase AC–AC Matrix Converter and Voltage DC-Link Back-to-Back Converter Systems," *IEEE Trans. Ind. Electron.*, vol. 59, no. 12, pp. 4487-4510, Dec. 2012.

[8] S. Nagai *et al*., "A 3-Phase AC–AC Matrix Converter GaN Chipset With Drive-by-Microwave Technology," *IEEE J. Electron Devices Soc*., vol. 3, no. 1, pp. 7-14, Jan. 2015.

[9] "U1000 Industrial Matrix Drive - Technical Manual" Manual No. SIEP C710636 04D, 2016.

[10] Y. Bak and K. -B. Lee, "Constant Speed Control of a Permanent-Magnet Synchronous Motor Using a Reverse Matrix Converter Under Variable Generator Input Conditions," *IEEE J. Emerg. Sel. Topics Power Electron.*, vol. 6, no. 1, pp. 315-326, March. 2018.

[11] L. Wang et al., "A Finite Control Set Model Predictive Control Method for Matrix Converter With Zero Common-Mode Voltage," *IEEE J. Emerg. Sel. Topics Power Electron.*, vol. 6, no. 1, pp. 327-338, March. 2018.

[12] W. Deng, "Maximum Voltage Transfer Ratio of Matrix Converter Under DTC With Rotating Vectors," *IEEE Trans. Power Electron.*, vol. 36, no. 6, pp. 6137-6141, June. 2021.

[13] J. Rodriguez, M. Rivera, J. W. Kolar and P. W. Wheeler, "A Review of Control and Modulation Methods for Matrix Converters," *IEEE Trans. Ind. Electron.*, vol. 59, no. 1, pp. 58-70, Jan. 2012.

[14] J. W. Kolar, F. Schafmeister, S. D. Round and H. Ertl, "Novel Three-Phase AC–AC Sparse Matrix Converters," *IEEE Trans. Power Electron.*, vol. 22, no. 5, pp. 1649-1661, Sept. 2007.

[15] O. Ellabban, H. Abu-Rub and S. Bayhan, "Z-Source Matrix Converter: An Overview," *IEEE Trans. Power Electron.*, vol. 31, no. 11, pp. 7436-7450, Nov. 2016.

[16] A. M. Bozorgi, A. Hakemi, M. Farasat and M. Monfared, "Modulation Techniques for Common-Mode Voltage Reduction in the Z-Source Ultra Sparse Matrix Converters," *IEEE Trans. Power Electron.*, vol. 34, no. 1, pp. 958-970, Jan. 2019.

[17] M. Guo, Y. Liu, B. Ge and H. Abu-Rub, "Optimum Boost Control of Quasi-Z Source Indirect Matrix Converter," *IEEE Trans. Ind. Electron.*, vol. 65, no. 10, pp. 8393-8404, Oct. 2018.

[18] M. Y. Lee, P. Wheeler and C. Klumpner, "Space-Vector Modulated Multilevel Matrix Converter," *IEEE Trans. Ind. Electron.*, vol. 57, no. 10, pp. 3385-3394, Oct. 2010.

[19] S. Tewari and N. Mohan, "Matrix Converter Based Open-End Winding Drives With Common-Mode Elimination: Topologies, Analysis, and Comparison," *IEEE Trans. Power Electron.*, vol. 33, no. 10, pp. 8578-8595, Oct. 2018.

[20] U. Nasir, A. Costabeber, P. Wheeler, M. Rivera and J. Clare, "A Three-Phase Modular Isolated Matrix Converter," *IEEE Trans. Power Electron.*, vol. 34, no. 12, pp. 11760-11773, Dec. 2019.

[21] M. Raghuram, A. K. Chauhan, and S. K. Singh, "High-gain-integrated switched capacitor indirect matrix converter," *IEEE J. Emerg. Sel. Top. Power Electron.*, vol. 7, no. 3, pp. 1846–1853, Sep. 2019.

[22] H. Wang, M. Su, Y. Sun, J. Yang, G. Zhang, W. Gui, and J. Feng, "Two-Stage Matrix Converter Based on Third-Harmonic Injection Technique," *IEEE Trans. Power Electron.*, vol. 31, no. 1, pp. 533-547, Jan. 2016.

[23] T. B. Soeiro, F. Vancu and J. W. Kolar, "Hybrid Active Third-Harmonic Current Injection Mains Interface Concept for DC Distribution Systems," *IEEE Trans. Power Electron.*, vol. 28, no. 1, pp. 7-13, Jan. 2013.

[24] L. Wang *et al*., "A Three-Level T-Type Indirect Matrix Converter Based

on the Third-Harmonic Injection Technique," *IEEE J. Emerg. Sel. Top. Power Electron*., vol. 5, no. 2, pp. 841-853, June. 2017.

[25] H. Wang *et al*., "Topology and Modulation Scheme of a Three-Level Third-Harmonic Injection Indirect Matrix Converter," *IEEE Trans. Ind. Electron*., vol. 64, no. 10, pp. 7612-7622, Oct. 2017.

[26] C. Lu, B. Zhou, J. Lei and J. Shan, "Mains Current Distortion Suppression for Third-Harmonic Injection Two-Stage Matrix Converter," *IEEE Trans. Power Electron*., vol. 36, no. 6, pp. 7202-7211, June 2021.

[27] C. Lu, B. Zhou, Q. Chang and J. Lei, "Improved Third-Harmonic Injection Two-Stage Matrix Converter Topology Based on Decomposition Control of Injection Current," *IEEE Trans. Power Electron*., vol. 37, no. 7, pp. 7846-7857, July 2022.

[28] Q. Chang, B. Zhou, C. Lu, and J. Wei, “Mains Current Distortion Analysis and Suppression Method for Third-Harmonic Injection Two-Stage Matrix Converter”, *IEEE Trans. Ind. Electron*., Early Access.